Remote Sensing of Environment 152 (2014) 467–479

Contents lists available at ScienceDirect

Remote Sensing of Environment

journal homepage: www.elsevier.com/locate/rse

An approach for the long-term 30-m land surface snow-free albedo retrieval from historic Landsat surface reflectance and MODIS-based a priori anisotropy knowledge

Yanmin Shuai [a,*], Jeffrey G. Masek [b], Feng Gao [c], Crystal B. Schaaf [d], Tao He [e]

[a] Earth Resources Technology, Inc., at Biospheric Science Laboratory (Code 618), NASA/GSFC, Greenbelt, MD 20771, USA
[b] Biospheric Science Laboratory (Code 618), NASA Goddard Space Flight Center, Greenbelt, MD 20771, USA
[c] Hydrology and Remote Sensing Laboratory USDA, Agricultural Research Service (ARS), Beltsville, MD 20705, USA
[d] School for the Environment, University of Massachusetts Boston, Boston, MA 02125, USA
[e] Department of Geographical Sciences, University of Maryland, College Park, MD 20742, USA

ARTICLE INFO

Article history:
Received 21 May 2014
Received in revised form 16 July 2014
Accepted 17 July 2014
Available online xxxx

Keywords:
Albedo algorithm
Landsat
MODIS BRDF
Forest disturbance

ABSTRACT

Land surface albedo has been recognized by the Global Terrestrial Observing System (GTOS) as an essential climate variable crucial for accurate modeling and monitoring of the Earth's radiative budget. While global climate studies can leverage albedo datasets from MODIS, VIIRS, and other coarse-resolution sensors, many applications in heterogeneous environments can benefit from higher-resolution albedo products derived from Landsat. We previously developed a "MODIS-concurrent" approach for the 30-meter albedo estimation which relied on combining post-2000 Landsat data with MODIS Bidirectional Reflectance Distribution Function (BRDF) information. Here we present a "pre-MODIS era" approach to extend 30-m surface albedo generation in time back to the 1980s, through an *a priori* anisotropy Look-Up Table (LUT) built up from the high quality MCD43A BRDF estimates over representative homogenous regions. Each entry in the LUT reflects a unique combination of land cover, seasonality, terrain information, disturbance age and type, and Landsat optical spectral bands. An initial conceptual LUT was created for the Pacific Northwest (PNW) of the United States and provides BRDF shapes estimated from MODIS observations for undisturbed and disturbed surface types (including recovery trajectories of burned areas and non-fire disturbances). By accepting the assumption of a generally invariant BRDF shape for similar land surface structures as *a priori* information, spectral white-sky and black-sky albedos are derived through albedo-to-nadir reflectance ratios as a bridge between the Landsat and MODIS scale. A further narrow-to-broadband conversion based on radiative transfer simulations is adopted to produce broadband albedos at visible, near infrared, and shortwave regimes. We evaluate the accuracy of resultant Landsat albedo using available field measurements at forested AmeriFlux stations in the PNW region, and examine the consistency of the surface albedo generated by this approach respectively with that from the "concurrent" approach and the coincident MODIS operational surface albedo products. Using the tower measurements as reference, the derived Landsat 30-m snow-free shortwave broadband albedo yields an absolute accuracy of 0.02 with a root mean square error less than 0.016 and a bias of no more than 0.007. A further cross-comparison over individual scenes shows that the retrieved white sky shortwave albedo from the "pre-MODIS era" LUT approach is highly consistent ($R^2 = 0.988$, the scene-averaged low RMSE = 0.009 and bias = −0.005) with that generated by the earlier "concurrent" approach. The Landsat albedo also exhibits more detailed landscape texture and a wider dynamic range of albedo values than the coincident 500-m MODIS operational products (MCD43A3), especially in the heterogeneous regions. Collectively, the "pre-MODIS" LUT and "concurrent" approaches provide a practical way to retrieve long-term Landsat albedo from the historic Landsat archives as far back as the 1980s, as well as the current Landsat-8 mission, and thus support investigations into the evolution of the albedo of terrestrial biomes at fine resolution.

1. Introduction

Surface albedo, defined as the ratio of radiant flux reflected from the Earth's surface to the incident flux, has been documented by the Global Terrestrial Observing System (GTOS) as one of the essential climate variables governing Earth's surface energy budget (Pinty et al., 2008; Schaaf, Cihlar, Belward, Dutton, & Verstraete, 2009; Schaaf et al., 2008). The radiative forcing intercepted by the land surface is perhaps the most important initial energy source for biophysical processes, through a further conversion into latent, sensible, and stored heat terms and input to the soil–vegetation biophysical system (Betts,

* Corresponding author.
E-mail address: shuaiym@gmail.com (Y. Shuai).

http://dx.doi.org/10.1016/j.rse.2014.07.009
0034-4257/

2000; Lyone, Jin, & Randerson, 2008; Ollinger et al., 2008; Peckham, Ahl, Serbin, & Gower, 2008; Randerson et al., 2006; Sellers, Los, et al., 1996; Sellers, Randall, et al., 1996; Zhang et al., 2009). Studies have shown that land cover change (and ecosystem disturbance) may have a significant influence on regional albedo, and hence long-term climate forcing (Bala et al., 2007; Betts, 2000; Claussen, Brovkin, & Ganopolski, 2001; Randerson et al., 2006). Terrestrial albedo varies enormously in space and time as a result of both natural events (e.g. weather disaster, insect, disease, wild fire, season-shifts, and vegetation phenological phase) and human activities (e.g. forest-thinning & clearing, crops-sowing & harvesting, urbanization, and other land use management methods) (Jin & Roy, 2005; Ju, Roy, Shuai, & Schaaf, 2010; O'Halloran, et al., 2011; Shuai and Schaaf, 2010; Shuai, Schaaf, et al., 2013; Shuai, Xie, Wang, & Wu, 2013; Xu et al., 2013). As strategies emerge for managing ecosystem carbon in order to mitigate global warming, several studies have pointed out the potential risk of ignoring the physical consequences of land cover change, including changes to land surface albedo (Betts, 2000; Lyone et al., 2008; Peckham et al., 2008; Randerson et al., 2006).

Albedo datasets have been derived from existing coarse-resolution satellite sensors to parameterize global land surface and climate models. Compared with previous single-angle models, modern albedo algorithms rely on multiple directional reflectance measurements to first estimate a Bi-directional Reflectance Distribution Function (BRDF) model of the target, then integrate over incident and view hemispheres to calculate albedo. Studies have concluded that relative errors can reach up to 45% without the consideration of direction/angle effects in the albedo estimation (Kimes & Sellers, 1985; Kimes, Sellers, & Newcomb, 1987). Because most satellite sensors cannot collect multiple observations of a target in a single pass, the sequential accumulation of data over multiple days (for sun-synchronous orbit) or multiple hours (geostationary orbit), may be adopted as a relevant solution to achieve multi-angle measurements sampling the full sun–target–sensor geometry. Global surface albedo has been mapped from the Advanced Very High Resolution Radiometer (AVHRR) (Csiszar & Gutman, 1999; Key, Wang, Stroeve, & Fowler, 2001), Earth Radiation Budget Experiment (ERBE) radiometer data (Li & Garand, 1994), and the Along Track Scanning Radiometer (ATSR). With the advent of routine albedo products retrieved from Polarization and Directionality of the Earth's Reflectances (POLDER-I and II) (Bicheron & Leroy, 2000; Hautecoeur & Leroy, 1998; Leroy et al., 1997; Maignan, Breon, & Lacaze, 2004), Multi-angle Imaging SpectroRadiomenter (MISR) (Martonchik, Pinty, & Verstraete, 2002; Martonchik et al., 1998), Clouds and the Earth's Radiant Energy System (CERES) (Rutan et al., 2009), Meteosat Visible and Infrared Imager (MVIRI)/Meteosat and Meteosat Second Generation (MSG) (Carrer, Roujean, & Meurey, 2010; Geiger, Carrer, Franchisteguy, Roujean, & Meurey, 2008; Pinty et al., 2000), SPOT4/VEGETATION (Franchistéguy, Geiger, Roujean, & Samain, 2005), and the recently launched Visible Infrared Imager Radiometer Suite (VIIRS) (Justice et al., 2013; Liang, Yu, & Defelice, 2005), albedo maps with spatial resolutions of 500-m to tens of kilometer and temporal frequencies of daily to monthly are now available to serve for climate model refining and inter-annual exploration (Schaaf et al., 2008).

While global climate studies can utilize the coarse-resolution surface albedo datasets described above, there remains a need for consistent, fine-resolution albedo products for specific applications. Several publications have highlighted the importance of land cover change, including deforestation, afforestation, agricultural expansion, urbanization, and other human-induced land surface alteration, to the terrestrial carbon cycle and climate changes (Goward et al., 2008; Masek & Collatz, 2006; Pan et al., 2011; Randerson et al., 2006). However, spatial resolutions coarser than 250-m may be insufficient to capture patch-scale vegetation changes associated with human land use and forest disturbance (Townshend and Justice 1988; Masek et al., 2013). Fine resolution imagery (~30 m or better) can more accurately quantify the areas and rates of these anthropogenic land changes. In addition, for climate change investigations, long time series of albedo products are required. Although operational albedo datasets covering the last 30 years have been assembled from different sensors covering different periods, the merging of multiple records raises issues of data consistency and quality. Because of the differences among sensors (wavelength of spectral bands, orbit geometry, spatial resolution, and geographic region), the derived albedo products may differ depending on the specific product, the data source, and the production strategies (Schaaf et al., 2009). Therefore, datasets derived from a single continuous acquisition program offers a greater potential for consistency in data quality. Despite differences in sensor design over time, the Landsat program has acquired a 42-year record of Earth Observations that captured global land conditions and dynamics through six successful missions since 1972. With the launch of Landsat-8 in February 2013 (Loveland & Dwyer, 2012), this record has the potential of reaching 50 years. The opening of the Landsat archive for free distribution in late 2008 has invigorated the push for creating long-term biophysical and land cover products from new and archived Landsat data (Woodcock et al., 2008; Wulder, Masek, Cohen, Loveland, & Woodcock, 2012). It includes this effort to develop the long-term, consistent surface albedo products from the Landsat program.

In a previous study, we developed a "concurrent" approach for generating 30-m resolution albedo products for the post-2000 (MODIS) era by combining Landsat surface reflectance with MODIS surface anisotropy information (Shuai, Masek, Gao, & Schaaf, 2011). In this study, we propose and validate a new approach to generate Landsat albedo products for the pre-MODIS era, by using albedo-to-nadir reflectance ratios (Shuai et al., 2011) and an a priori anisotropy Look-Up Table (LUT) that has been built up from the high quality MCD43A BRDF retrievals over representative homogeneous regions. This approach yields both spectral and broadband albedos, and a quality assessment (QA) map based on the quality of MODIS anisotropy and Landsat surface reflectance. In this paper, we first address the theoretical basis of the "pre-MODIS-era" LUT approach, creation of the BRDF-LUT, and then demonstrate its application over more than 100 Landsat scenes in the Pacific Northwest of the United States where simultaneous ground measurements are available for validation.

2. Albedo definition

The spectral Directional–Hemispherical Reflectance (DHR) of a plane surface is defined as the ratio of radiant energy scattered upward from the surface in all directions to the down-welling incident irradiance on the surface within the target spectrum regime (λ_1, λ_2). It equals the integral of the BRDF over the view hemisphere for an incident beam at a given wavelength, as shown in formula (1). Under the extreme condition that no diffuse radiation but only the direct beam arrives from the solar incidence angle (θ, φ) defined by zenith angle θ, and azimuth angle φ ($L(\theta, \varphi)$), the albedo is referred to as "Black-Sky Albedo" (BSA) $\overline{R}(\theta_i, \varphi_i; \lambda)$ in the MODIS product series (Lucht, Schaaf, & Strahler, 2000; Strahler et al., 1999). Under the assumption that all irradiance is isotopic (purely diffuse skylight), a further integral over illumination hemisphere provides the Bi-Hemispherical Reflectance (BHR) $\overline{\overline{R}}(\lambda)$, or "White-Sky Albedo" (WSA) formulae (2) and (3) (Lucht et al., 2000; Strahler et al., 1999). The spectral BHR under actual atmospheric conditions (known as the "blue-sky albedo", or "actual albedo") can be approximated through a linear combination of BSA and WSA, weighted by the fraction of actual direct to diffuse skylight (Lewis & Barnsley, 1994; Lucht et al., 2000; Román et al., 2010). Because the upwelling radiance depends on not only the BRDF properties of the observed surface, but also atmospheric conditions, $\overline{\overline{R}}(\lambda)$ may change with the variation of the instantaneous cloud cover and aerosol loading, as well as over the course of the day as the solar geometry changes even for constant atmospheric and surface conditions (Lucht et al., 2000). In addition, multiple scattering between surface and atmosphere affects the angular distribution

of sky radiance. Therefore, bi-hemispheric reflectance (i.e. albedo) is not a true surface property, but rather a function of solar beam direction, atmospheric state, and surface anisotropic features.

$$\begin{aligned}\overline{R}(\theta_i,\varphi_i;\ \lambda) &= \int_0^{2\pi}\int_0^{\pi/2} f_r(\theta_i,\varphi_i;\theta_v,\varphi_v;\lambda)\cos\theta_v \sin\theta_v d\theta_v d\varphi_v \\ &= \frac{1}{\pi}\int_0^{2\pi}\int_0^{\pi/2} R(\theta_i,\varphi_i;\theta_v,\varphi_v;\ \lambda)\cos\theta_v \sin\theta_v d\theta_v d\varphi_v\end{aligned} \tag{1}$$

where $\overline{R}(\theta_i,\varphi_i;\ \lambda)$ = Spectral black-sky albedo (Directional–Hemispherical Reflectance, DHR) as a function of the solar incidence angle (θ_i, φ_i) (Strahler et al., 1999), and $f_r(\theta_i, \phi_i; \theta_v, \phi_v; \lambda)$ = Bidirectional Reflectance Distribution Function (BRDF) describing the behavior of surface scattering as a function of a parallel incident beam from one direction (θ_i, ϕ_i) in the illuminating hemisphere into the reflected direction (θ_v, ϕ_v) in the viewing hemisphere, at a particular wavelength λ. Further elaboration is presented in Nicodemus, Richmond, Ginsberg, and Limperis (1977) and Schaepman-Strub, Schaepman, Painter, Dangel, and Martonchik (2006). The terms "BRDF" and "anisotropy" in this paper refer to this underlying property.

$$\begin{aligned}\overline{\overline{R}}(\lambda) &= \frac{\int_0^{2\pi}\int_0^{\pi/2}\left(\int_0^{2\pi}\int_0^{\pi/2} f_r(\theta_i,\varphi_i;\theta_v,\varphi_v;\lambda)\cos\theta_v \sin\theta_v d\theta_v d\varphi_v\right) L_i(\theta_i,\varphi_i;\lambda)\cos\theta_i \sin\theta_i d\theta_i d\varphi_i}{\int_0^{2\pi}\int_0^{\pi/2} L_i(\theta_i,\varphi_i;\lambda)\cos\theta_i \sin\theta_i d\theta_i d\varphi_i} \\ &= \frac{\int_0^{2\pi}\int_0^{\pi/2} \overline{R}(\theta_i,\varphi_i;\lambda) L_i(\theta_i,\varphi_i;\lambda)\cos\theta_i \sin\theta_i d\theta_i d\varphi_i}{\int_0^{2\pi}\int_0^{\pi/2} L_i(\theta_i,\varphi_i;\lambda)\cos\theta_i \sin\theta_i d\theta_i d\varphi_i}\end{aligned} \tag{2}$$

$$\overline{\overline{R_{WSA}}}(\lambda) = \frac{1}{\pi}\int_0^{2\pi}\int_0^{\pi/2} \overline{R}(\theta_i,\varphi_i;\lambda)\cos\theta_i \sin\theta_i d\theta_i d\varphi_i \tag{3}$$

Strictly speaking, for natural targets, BRDF or any other nominal directional-related metric is not a measurable quantity, as it requires perfectly collimated beams of illumination and observation, while actual sunlight is partly diffuse and the measurements involve conical geometries. Thus, individual satellite measurement provides only an approximation of the directional reflectance.

For most of the applications involving energy balance, the reflectance quantity of interest is not the spectral reflectance but rather reflectance integrated over a broad spectral interval (λ_1, λ_2), see formula (4), to capture the overall radiative forcing. The spectral integrals for the hemispherical reflectance are functions of the down-welling solar spectrum as defined in the above formulae. The visible regime (0.3–0.7 μm) known as photosynthetically-active radiation (PAR) is of special interest to carbon cycle modelers for the estimation of carbon fixation via photosynthesis (Dorman & Sellers, 1989). In contrast, the total shortwave regime (0.3–3.0 μm), as well as visible and near-infrared bands, are typically required by surface energy balance studies. Note that the generic term "albedo", without any specification of the sun-view geometry and integral wavelength, often implies the bi-hemispheric broadband albedo of the whole solar irradiance domain.

$$\overline{\overline{R}}(\lambda_1\rightarrow\lambda_2) = \frac{\int_{\lambda_1}^{\lambda_2}\left(\int_0^{2\pi}\int_0^{\pi/2}\left(\int_0^{2\pi}\int_0^{\pi/2} f_r(\theta_i,\varphi_i;\theta_v,\varphi_v;\lambda)\cos\theta_v \sin\theta_v d\theta_v d\varphi_v\right) L_i(\theta_i,\varphi_i;\lambda)\cos\theta_i \sin\theta_i d\theta_i d\varphi_i\right) d\lambda}{\int_{\lambda_1}^{\lambda_2}\left(\int_0^{2\pi}\int_0^{\pi/2} L_i(\theta_i,\varphi_i;\lambda)\cos\theta_i \sin\theta_i d\theta_i d\varphi_i\right) d\lambda} \tag{4}$$

3. Algorithm

The initial impetus to develop a "pre-MODIS era" approach flowed from the desire to understand albedo consequences of specific types of forest disturbance and recovery at a fine resolution. To extend 30-m surface albedo generation in time back to the 1980s, we first build an a priori anisotropy Look-Up Table (LUT) from the high quality MCD43A BRDF estimates over representative homogenous regions, then calculate the albedo-to-nadir reflectance ratios for each entry and apply these ratios to the 30-m Landsat nadir reflectance. Finally, we use narrow- to broad-band conversion factors to derive broadband Landsat albedos. Fig. 1 outlines the overall workflow of this approach into three main functional components: surface reflectance calculation and assessment (Fig. 1A), BRDF-LUT creation (Fig. 1B), and Landsat surface albedo generation (Fig. 1C). The aim of "surface reflectance calculation and assessment" is to retrieve terrain and atmosphere corrected surface reflectance (that is defined in Masek et al., 2006) from the Landsat Thematic Mapper and Enhanced Thematic Mapper Plus (TM/ETM+) L1T, and remove pixels contaminated by cloud and snow from further analysis. The aim of "BRDF-LUTs creation" is to build up the a priori anisotropy information for each defined land surface category from the operational MODIS 500-m high quality anisotropy products (i.e. MCD43A) over representative homogeneous land surface structure regions. The aim of "Landsat albedo generation" is to obtain the narrow-band spectral albedo by combining Landsat directional surface reflectance with the specific a priori anisotropy information stored in the BRDF-LUTs, and then convert narrow to broad band albedos for the visible (0.3–0.7 μm), NIR (0.7–3.0 μm), and shortwave (0.3–3.0 μm) regimes.

3.1. Surface reflectance assessment

Landsat surface directional reflectance at each spectral band of Thematic Mapper and Enhanced Thematic Mapper Plus (TM/ETM+) has

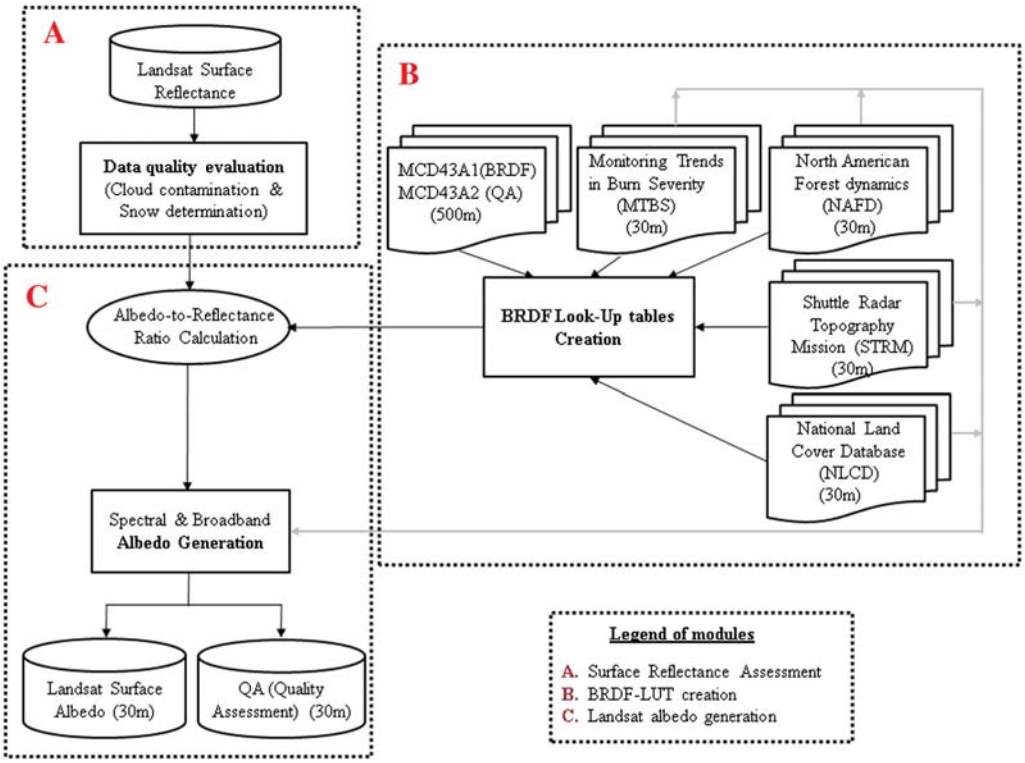

Fig. 1. Flow chart of the "pre-MODIS era" LUT approach composed of three functional components (A. surface reflectance assessment; B. BRDF-LUT creation; and C. Landsat albedo generation).

been produced from orthorectified Landsat level 1 T raw images downloaded from *USGS EROS*, using the Landsat Ecosystem Disturbance Adaptive Processing System (LEDAPS) (Masek et al., 2006). The level 1 raw radiometry data ingested by LEDAPS were calibrated to at-sensor radiance, converted to top-of-atmosphere reflectance, and then atmospherically corrected to surface reflectance using the second simulation of satellite signal in the solar spectrum (6S) model (Masek et al., 2006; Vermote, Saleous, & Justice, 2002; Vermote et al., 1997). LEDAPS demonstrated good performance through comparisons with ground-based AERONET optical thickness measurements (Masek et al., 2006), concurrent MODIS Terra reflectance (Feng et al., 2012; Masek et al., 2006), and other approaches for Landsat surface reflectance generation (Ju, Roy, Vermote, Masek, & Kovalskyy, 2012). To mitigate the cloud effect on the surface radiometric accuracy, pixels contaminated by cloud, cloud shadow, and adjacent clouds were screened from this study using the LEDAPS-derived cloud mask. An additional screening for snow was performed based on the operational MODIS snow mapping algorithm (Hall, Riggs, Salomonson, DiGirolamo, & Bayr, 2002), through the Normalized Difference Snow Index (NDSI) calculated from reflectance at Landsat green (0.53–0.61 μm) and shortwave infra-red (1.55–1.75 μm) bands. Further thresholds for green band reflectance (>0.10) and NDVI were applied to reduce the erroneous classification of very dark targets (such as black spruce forests), as well as the thermal mask to eliminate the spurious snow cover possibly induced by residual cloud cover, aerosol effect and snow/sand confusion on coastlines (Hall, Riggs, & Salomonson, 1995; Hall et al., 2002).

3.2. BRDF Look-Up Tables

The most direct way to obtain anisotropy information of any land surface target at the pixel scale is to collect a representative sample of reflectance observations at multiple directions, over a short interval of time. However, because of the narrow field of view of Landsat (±7.5 degrees) and the limited number of acquisitions offered by the 16-day repeat cycle, it is not feasible to obtain target anisotropy information directly from multiple Landsat directional reflectance observations. Instead, we need to obtain target BRDF estimates from other sources, such as MODIS, or MISR.

For this study, the Collection V005 MODIS 8-day anisotropy dataset (MCD43A) was used to create the BRDF-LUT because of its wide range of sun and view angles, the broad spectral coverage of MODIS for simultaneous atmosphere correction, frequent acquisition for the potential daily adjustment of BRDF retrieval, the 500-m moderate resolution, and especially the continuity of global products since 2000. The operational MODIS albedo and reflectance anisotropy products make use of the kernel-driven, linear algorithm that relies on the weighted sum of an isotropic and two additional kernels (respectively called Ross-thick and Li-sparse-reciprocal models, RTLSR) of viewing and illumination geometry to estimate the BRDF model (Li & Strahler, 1992; Lucht et al., 2000; Ross, 1981; Roujean, Leroy, Podaire, & Deschamps, 1992). The retrieved kernel weights (also called BRDF model parameters) are those that best fit an adequate angular sample of the high quality cloud-cleared, atmospherically corrected surface reflectances available for each pixel over a 16-day period (Lucht et al., 2000; Schaaf et al., 2002, Schaaf, Liu, Gao, & Strahler, 2011; Shuai, Schaaf, Strahler, Liu, & Jiao, 2008; Shuai & Schaaf, 2010). This model combination has been shown to be well-suited to describe the surface anisotropy of the variety of land surfaces distributed worldwide (Privette, Eck, & Deering, 1997). The absolute accuracy of MCD34A albedo at local solar noon (LSN) derived from the estimated BRDF model has been established by comparison with ground measurements from available international Baseline Surface Radiation Network (BSRN) and Fluxnet sites (Cescatti et al., 2012; Román et al., 2009; Wang et al., 2014). This algorithm assumes that the land surface does not experience significant structural changes during the 16-day observation period, which is reasonable except in circumstances of abrupt disturbance or conversion.

The creation of a BRDF LUT is based on the identification of land surface intrinsic anisotropic features which make one object distinguishable from others. Numerous studies have demonstrated unique anisotropic

Table 1
Structure of the BRDF LUT.

Type	Land cover class #	Disturbance age	Disturbance severity	Month	DEM	QA	Bands (1–5, 7)	RTLS-R parameters
Range of value	NLCD classification scheme	0–30	Low, medium, or high	1–12	Flat or mountainous	0–5	Landsat 1–5, 7	Isotropic, volumetric, and geometric kernel weights
Un-disturbed	✓	NA	NA	✓	✓	✓	✓	✓
Fire-disturbed	✓	✓	✓	✓	NA[a]	✓	✓	✓
Nonfire-disturbed	✓	✓	NA[a]	✓	NA[a]	✓	✓	✓

[a] Limited by the lack of current ancillary data community.

features among distinct landscape attributes (Bacour & Bréon, 2005; Bicheron & Leroy, 2000; Lovell & Graetz, 2002; Maignan et al., 2004; Shuai & Schaaf, 2010; Strugnell & Lucht, 2001), biome components (Chen & Leblanc, 1997), vegetation life-cycle and seasonal stages (Kimes, 1983; Shuai et al., 2011), and classes of disturbance induced by natural or human activity, as well as significant effects from terrain (Schaaf, Li, & Strahler, 1994). Thus, the attributes defined in Table 1 are adopted to build the overall conceptual structure of BRDF-LUT. Each entry in the LUT reflects a unique combination of land surface type, terrain, time of year, limited disturbance age and type, and Landsat spectral bands.

Several ancillary datasets provided the basis for this stratification. First, the 30-m 2006 NLCD (National Land Cover Database, Vogelmann, Sohl, & Howard, 1998) classification maps with high overall and user's accuracy (Wickham et al., 2013) were used to determine local landscape attributes, and to identify representative homogenous land surface regions when aggregated to the MODIS 500-m resolution. Then, two datasets giving the timing and location of ecosystem disturbance were used to quantify the BRDF evolution of disturbed landscapes. The annual 30-m Monitoring Trends in Burn Severity (MTBS) (Eidenshink et al., 2007) dataset has mapped the low/medium/high burn severity of fires (greater than 1000 acres in the west and 500 acres in the east) that have occurred since 1984 across all lands of the United States. The 30-m NAFD (North American Forest Dynamics, Masek et al., 2008; Masek et al., 2013; Huang et al., 2010) dataset identified other forest non-fire disturbance events (such as harvest, storm damage, or disease) over the same time period. While the NAFD dataset targets rapid disturbance events that remove substantial canopy cover, more subtle or gradual declines in live biomass (e.g. selective tree removal, gradual insect outbreaks) may not be captured. Both MTBS and NAFD datasets are generated from Landsat spectral signatures before and after the disturbance events. While the MTBS dataset uses independent confirmation of fire

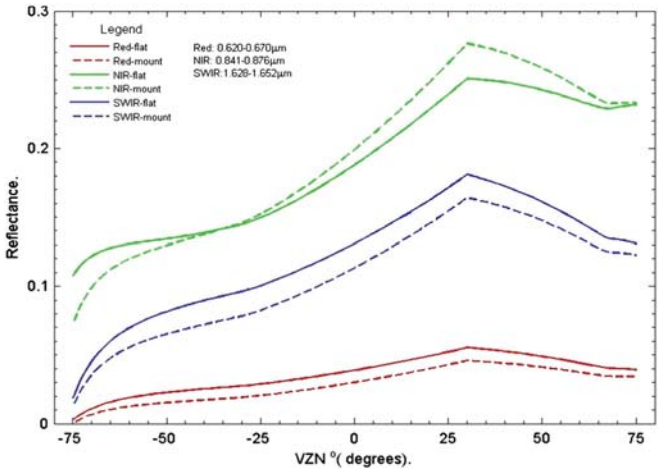

Fig. 2. Example of the difference in MODIS BRDF shape estimated for non-disturbed evergreen forest (in principle plane at 30° solar zenith angle) obtained from a mountainous region (slope > 15°, dot-line) and a relatively flat region (slope ≤ 15°, solid line) at NIR (upper), SWIR (middle), and Red (lower) bands from the Pacific Northwest region of the United States.

timing (from the National Interagency Fire Center), the NAFD dataset may have one or two year bias on the timing of disturbance if a cloud-free image or composite was not produced for a given year. Since both datasets cover the period since 1984, any fire and non-fire disturbance events encountered before the Landsat TM/ETM + era (1980s) are not be defined in the maps. In addition, the Shuttle Radar Topography Mission (SRTM) DEM data (Farr et al., 2007) was utilized to differentiate the quality of BRDF shapes affected by mountainous terrain. Due to the study in Schaaf et al. (1994) in terrain effects on the anisotropy feature, the MODIS estimated BRDFs were qualitatively graded into two strata (flat to moderate with slope ≤ 15°; and steeper mountainous with slope > 15°). An example is shown in Fig. 2 for individual undisturbed evergreen needle leaf forest patches respectively in a flat region and a high-slope mountainous region.

Thus the a priori BRDF LUTs for the Pacific Northwest (PNW) region of United States were created from MCD43A products and ancillary datasets (see module B in Fig. 1) in terms of the above conceptual structure of the BRDF LUT. The PNW was selected for this initial prototype due to its range of ecosystems, prevalence of both fire- and non-fire forest disturbances, and range of topography. In order to minimize the effect of biome mixtures, MODIS 500-m pixels were labeled as representative "pure" pixels if they were composed of at least 85% of a single land surface type when aggregated from the 30-meter NLCD land cover map. In addition to being stratified by NLCD land cover, the LUT of BRDF was also stratified by disturbance type ("undisturbed", "fire disturbed", "non-fire disturbance"), disturbance severity (from the MTBS fire disturbance product), topographic slope (greater or less than 15°), time since disturbance (0–26 years corresponding to the NAFD and MTBS coverage of 1984–2010), and month of the year (Table 1). For each combination of these attributes, the BRDF shapes for Landsat (and MODIS) reflective bands were extracted from the operational V005 8-day MCD43A1 (BRDF parameters) and MCD43A2 (QA flags) 11-year product (Schaaf et al., 2002; Shuai et al., 2008). The time dimension (month for the undisturbed LUT, and age of disturbance), was used to depict the seasonality, growth phase, and growth evolution since disturbance, in the BRDF shapes over for a given land surface scenario. If no high quality BRDF was available for a given month (for a seasonal characterization) or year (for characterizing post-disturbance evolution), a backup BRDF shape was established through linear interpolation of the BRDF model parameters from available time periods. To document the quality of BRDF shapes in the LUT, each was assigned a quality flag denoted as "high quality" for the original MCD43A estimation and "low quality" for those interpolated ones.

As an example, Fig. 3 shows the BRDF shapes in the principle plane with solar incident at 30° zenith angle, averaged over disturbed evergreen forest regions in the PNW. The snow-free time series of BRDF shapes from September illustrate the evolution of evergreen forest signature over two decades in the green, NIR, and SWIR bands. It is seen that BRDFs of both fire and non-fire disturbance types have systematic temporal variations in shapes and magnitudes. The evolution of this generalized BRDF-shape may be associated with regrowth and recovery of canopy greenness and structure for the disturbed forest land, indicated by the gradual sharpening or flattening of the hot-spot. There are strong temporal signatures of green vegetation in both examples of the disturbance types, firstly displayed as a clear enhanced hot-spot in

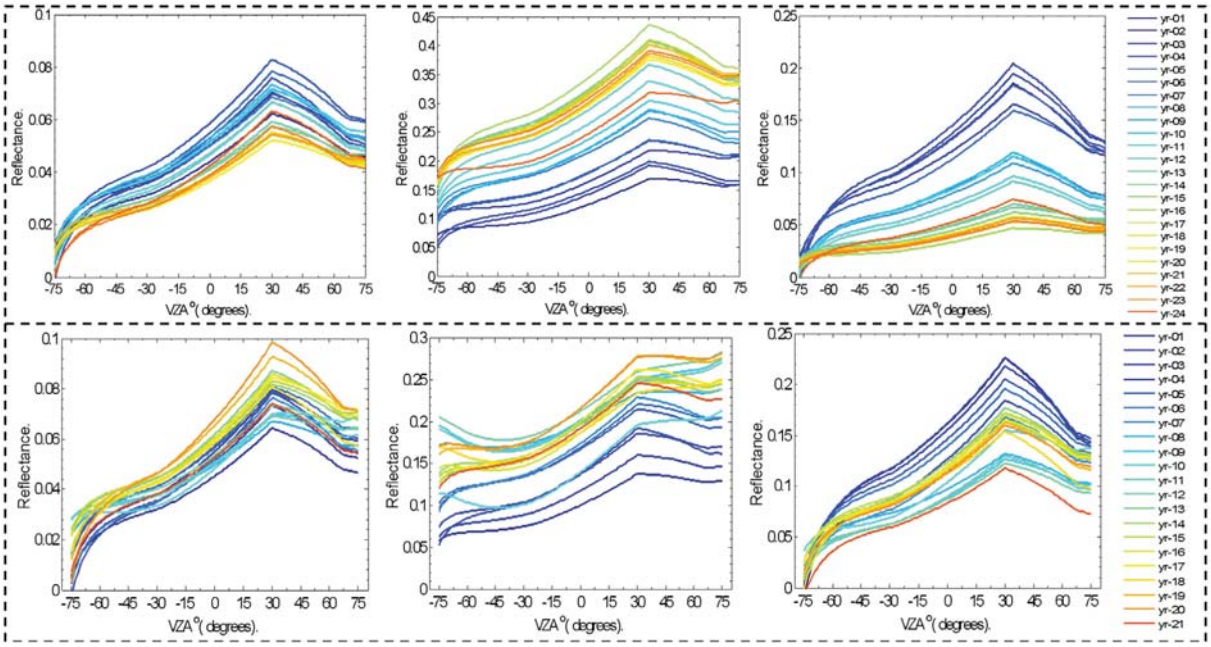

Fig. 3. Two decades of BRDF evolution following non-fire disturbance (harvest, thinning dominated, top panels) and high-severity fire disturbance (bottom panels) in the Pacific Northwest of the United States, for green (left), near-infrared (middle), and shortwave-infrared (right) bands. The original MCD43A BRDF shapes were retrieved from September in the principle plane with solar incident at 30° zenith angle. The BRDF shapes show a strong hot-spot in the backward (showing as positive view zenith angle—VZA) direction, and systematic changes in magnitude and shape following disturbance events.

the NIR band with the increasing of greenness, and a suppression of the hot-spot at the SWIR with the augmentation of canopy water content accompanying the forest regrowth. In contrast to the monotonic decrease in brightness following non-fire disturbance, the high-burn-severity fire disturbed forest presents a complicated trajectory of anisotropy development in the green band, with a multiple-year (~7–12 years since disturbance) reduction during the increase of the hot-spot. It may be explained by the different recovery trajectories of the post-fire residual structures. These post-fire residual transition rates will vary among fires, with a high rate in the first two years from tree to snag (i.e. tree mortality), and a late peak after several years later for the tree-to-downed wood and snag-to-downed wood change depending on the species and tree size of the burned forest region. Once the green signature from the re-grown forest and understory vegetation (such as grass or shrub) becomes dominant, a continuous gradual increasing can be captured generally 10 years after severe fires, as shown in Fig. 3. Some small fluctuations found in the gradual evolution of each BRDF shape could be due to uncertainties in the mapped timing of disturbance, poorer quality BRDF estimation, variations in atmospheric conditions, and residual cloud and snow effects.

Table 2
Segments of the pixel-based 16-bit QA word for each Landsat albedo map to indicate the performance of albedo retrieval.

Bit	Meaning
b15	Fill value (1 = fill-value)
b14	Cloud flag (1 = cloud contamination)
b13	Snow flag (1 = snow contamination)
b12	Disturbance flag (0 = undisturbed; 1 = disturbed)
b11-10	Disturbance type (00 = fire; 01 = non-fire; 10 and 11 = reserved)
b9–8	Fire disturbance severity (00 = reserved; 01 = low; 10 = medium; 11 = high)
b7	BRDF QA (0 = original; 1 = backup/interpolation)
b6–0	Disturbance age for disturbed pixel or land cover class for un-disturbed pixel

3.3. Surface albedo determination

Once the BRDF shape is determined, surface albedo at 30-meter resolution can be calculated from the albedo-to-nadir reflectance ratio (A/N) and Landsat surface reflectance as detailed for the "concurrent" approach in Shuai et al. (2011). This method assumes that a given surface type has the same BRDF shape at MODIS or Landsat resolution, and can be scaled to albedo using the 30-meter directional reflectance from Landsat as shown in (5), with R_{lnd} and R_{mod} denoting the corresponding spectral reflectance from Landsat and MODIS, respectively. Then, the Landsat black-sky albedo with a solar zenith angle at the Landsat overpass time and white-sky albedo were computed respectively for the six non-thermal Landsat bands. The broadband albedos for visible (0.3–0.7 μm) α_{vis}, near infrared (0.7–3.0 μm) α_{nir}, and shortwave (0.3–3.0 μm) α_{short} bands were produced by a further conversion from narrow spectral band albedo values (α_i) using new conversion coefficients for Landsat 5 TM (6–8) and Landsat 7 ETM + (9–11). These coefficients were derived from radiative transfer simulations using 245 surface spectra representing different surface types (He, Liang, Wang, Shuai, & Yu, 2013; Liang, 2000). Finally, a quality assessment (QA) layer constructed into a 16-bit word was stored for each pixel (see Table 2) to track the quality of input data, and estimate error propagation through the fusion of multiple data sources.

$$\begin{cases} R_{mod}(\theta_{mod}=\theta\varphi_{mod}=\varphi_i;\theta_v,\varphi_v;\lambda)\approx R_{lnd}(\theta_{lnd}=\theta_i,\varphi_{lnd}=\varphi_i;\theta_v,\varphi_v;\lambda) \\ f_{r\_mod}(\theta_i,\phi_i;\theta_v,\phi_v;\lambda)=f_{r\_lnd}(\theta_i,\phi_i;\theta_v,\phi_v;\lambda) \end{cases}$$
$$\Rightarrow \begin{cases} \overline{R_{lnd}}(\lambda)=R_{lnd}(\theta_i,\varphi_i;\theta_v,\varphi_v)\times\dfrac{\overline{\overline{R_{mod}}}(\lambda)}{R_{mod}(\theta_i,\varphi_i;\theta_v,\varphi_v)} \\ \overline{R_{lnd}}(\theta_i,\varphi_i;\lambda)=R_{lnd}(\theta_i,\varphi_i;\theta_v,\varphi_v)\times\dfrac{\overline{R_{mod}}(\theta_i,\varphi_i;\lambda)}{R_{mod}(\theta_i,\varphi_i;\theta_v,\varphi_v)} \end{cases} \quad (5)$$

$$\alpha_{short}=0.3206\alpha_1+0.1572\alpha_3+0.3666\alpha_4+0.1162\alpha_5+0.0457\alpha_7-0.0063 \quad (6)$$

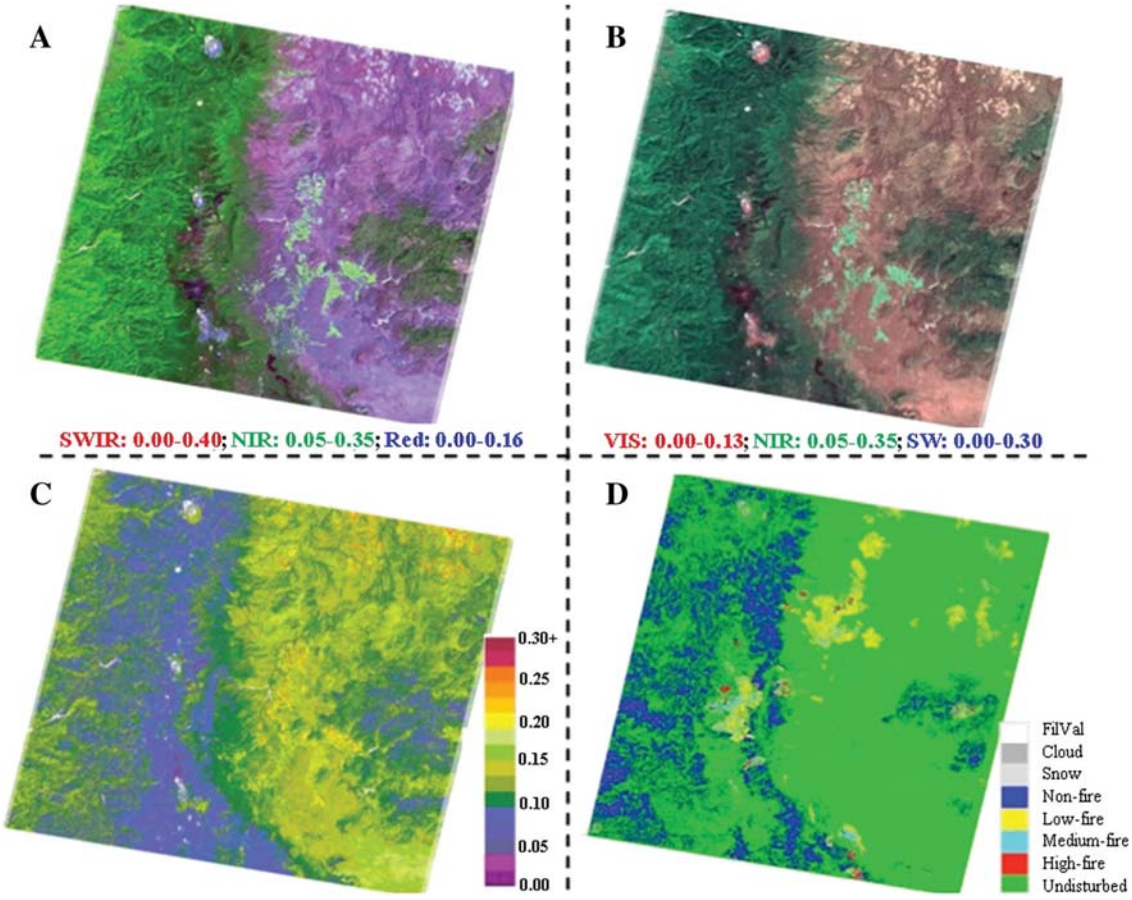

Fig. 4. Examples of the "pre-MODIS era" approach generated from scene (path/row: 45/29) on day 2007-08-29. (A) The spectral black-sky albedo composite of Landsat-5 bands 5, 4, and 3, (B) the broadband black-sky albedo composite of visible, near infrared, and shortwave bands, (C) the black-sky albedo for the shortwave band, and (D) the quality assessment maps.

$$\alpha_{vis} = 0.6000\alpha_1 + 0.2204\alpha_2 + 0.1828\alpha_3 - 0.0033 \quad (7)$$

$$\alpha_{nir} = 0.6646\alpha_4 + 0.2859\alpha_5 + 0.0566\alpha_7 - 0.0037 \quad (8)$$

$$\alpha_{short} = 0.3141\alpha_1 + 0.1607\alpha_3 + 0.3694\alpha_4 + 0.1160\alpha_5 + 0.0456\alpha_7 - 0.0057 \quad (9)$$

$$\alpha_{vis} = 0.5610\alpha_1 + 0.2404\alpha_2 + 0.2012\alpha_3 - 0.0026 \quad (10)$$

$$\alpha_{nir} = 0.6668\alpha_4 + 0.2861\alpha_5 + 0.0572\alpha_7 - 0.0042 \quad (11)$$

3.4. Central Oregon example for the derived Albedo and QA maps

Fig. 4 shows maps of the 30-m Landsat albedo products generated from the "pre-MODIS era" LUT approach for a scene in central Oregon (path/row: 45/29) on August 29, 2007. Spectral black-sky albedo estimates are provided as the composite of shortwave infrared, near infrared, and red bands (wavelength centered 1.65 μm, 0.83 μm, and 0.66 μm) (Fig. 4A). Broadband black-sky albedos are available for the visible (0.3–0.7 μm), near-infrared (0.7–3.0 μm), and shortwave (0.3–3.0 μm) bands (Fig. 4B and C). At the date corresponding to the selected sample case, a large part of the Central and Eastern region was dominated by sparse shrubs or barren land. Compared with the forest region in the central-west part, these areas appear as high values in the SWIR and Red bands, lower values in the NIR band, with scattered agricultural fields in the lower-central region and forest stands in the middle-eastern region in Fig. 4A. In the three-broadband composite image (Fig. 4B), however, the albedo in the visible regime has higher values than the other two bands and shows up as brown-red in the corresponding areas. For the retrieval of each pixel, one corresponding QA map (Fig. 4D) provides the possible cloud and snow contamination, and details of undisturbed or disturbed information.

4. Accuracy assessment of the Landsat albedo products

Three approaches have been used to evaluate the accuracy of albedo products generated by the "pre-MODIS era" LUT approach presented in this paper. One is the direct validation of shortwave albedo with actual ground measurements. The other two methods are cross-comparisons of surface albedo maps generated by (1) the "concurrent" approach of Shuai et al. (2011) that uses coincident MODIS products to retrieve Landsat-scale albedo, and (2) the coincident operational MODIS albedo products themselves. Comparison with ground measurements is an independent and optimal approach for product validation, but suffers from the limited availability of ground albedo-meter measurements. Cross-comparison with other products can be performed on a large volume of MODIS images, but does not provide a robust estimate of absolute accuracy. Utilization of these multiple validation means may increase the ability to evaluate the algorithm performance thoroughly and objectively.

4.1. Validation with ground measurements

Independent ground or tower albedo measurements are generally considered to be more accurate than satellite retrievals, and are often taken as a reference for the validation of satellite products. However,

Table 3
Forested ground stations in the Pacific Northwest region.Acquired from the network-wide AmeriFlux database.

Site name	Vegetation type	Location[a]	Tower height (m)	Canopy height (m)	Footprint of observation (m)[b]	Data period	Landsat retrieval #
US-Me2	ENF[c]	44°27′8.28″N, 121°33′25.92″W	32.0	~22	228.6	2005–2007; 2009–2011	32
US-Me3	ENF[c]	44°18′55.68″N, 121°36′28.29″W	18.0[d]	~3.11	342.9	2004–2009	4
US-Me6	ENF[c]	44°19′23.43″N, 121°36′15.69″W	18.6[e]	~7.0	265.2	2010–2011	7
US-NR1	MF[f]	40°1′58.31″N, 105°32′49.09″W	26	11.5	331.5	2006–2011[g]	24
US-GLE	Subalpine, alpine	41°21′59.51″N, 106°14′23.82″W	23/30[h]	12.1	249.2/409.2	2004–2011	24
US-Blk	Conifer	44°09′01″N, 103°38′24″W	24	13–15	251.5–205.7	2004–2009	24

[a] Location of each site is confirmed by their PIs via private communication.
[b] Diameter of ground measurements footprint in the horizontal plane at canopy height.
[c] Evergreen needle leaf forest.
[d] Tower height is 18 m, instrument CNR-1 is mounted at 14 m.
[e] Tower height is 18.6 m, instrument mounted at 17.7 m.
[f] Subalpine mixed coniferous forest.
[g] Currently only post 2005 ground data to be used in terms of data processor's suggestion via personal contact.
[h] Tower height is 30 m during 1999–2006, and adjusted to 23 m since 2006.

the validation of satellite-derived products is difficult because the footprint of satellite observations differs significantly from that of in-situ instruments. Only measurements spatially representing the surrounding landscape at both in-situ and satellite scales can provide a comparable basis for validation (Román et al., 2009).

4.1.1. Surface albedo ground measurements

Tower-based surface albedo measurements were acquired from six available forested sites of AmeriFlux network in the Pacific Northwest region of the United States (Table 3; Ruehr, Martin, & Law, 2012; Thomas et al., 2009; Vickers, Thomas, Pettijohn, Martin, & Law, 2012;

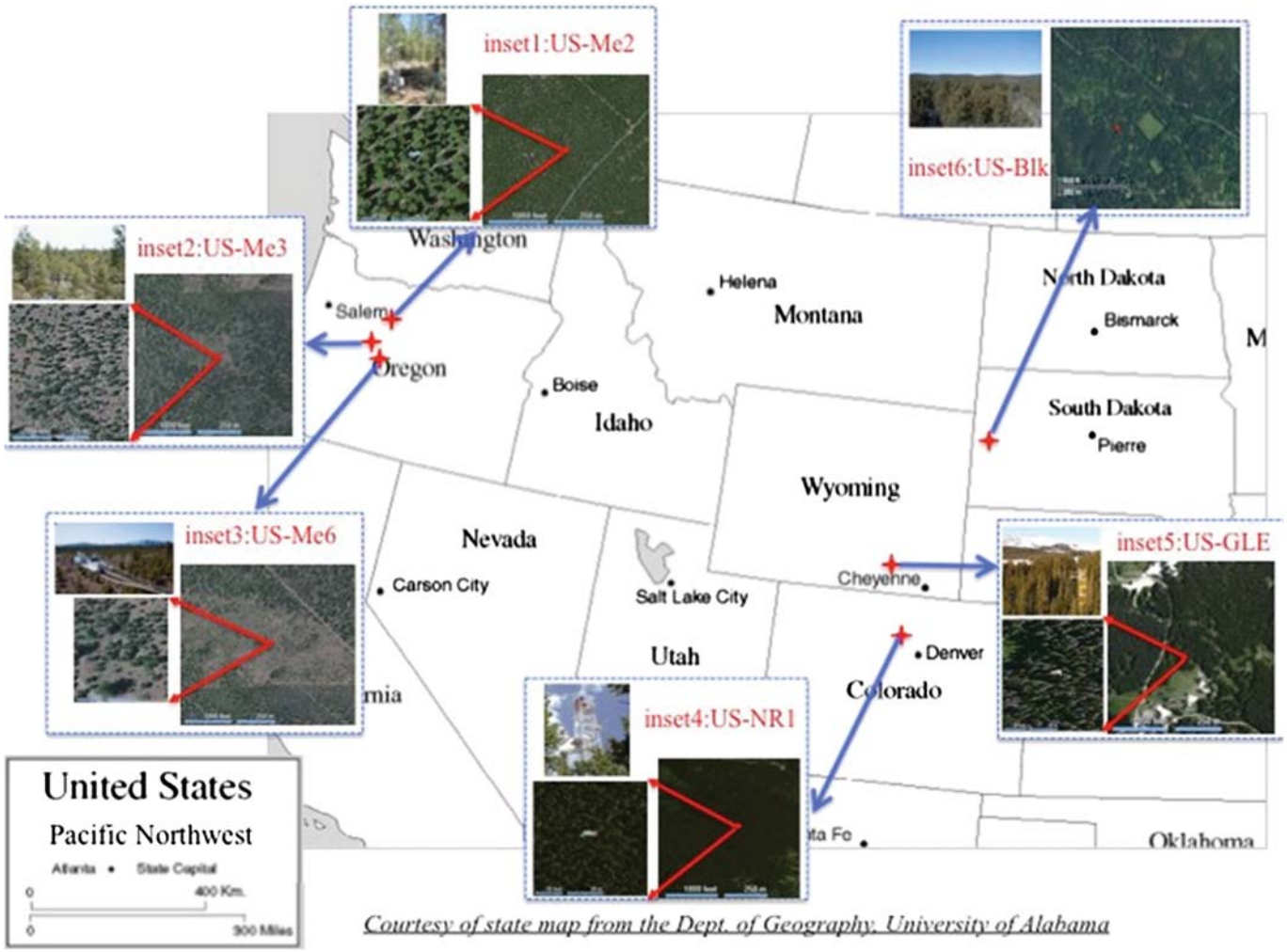

Fig. 5. Distribution of Ameriflux validation sites in the Pacific Northwest region of the United States. For each site, a ground photo (Upper-left), photo of tower surroundings (lower-left), and high-resolution satellite image (right) are shown. Note: image of tower surroundings for the currently deactivated US-Blk site is not available.

Wilson & Meyers, 2007). Forested sites were of particular interest since one of the overall objectives was to understand how forest disturbance and recovery influenced the albedo trajectories. The field sites sample forest ecosystems with different species composition, age and disturbance regimes (see the distribution and landscapes in Fig. 5), including sub-alpine forest older than 400 years with dispersed younger trees at the US-GLE site, subalpine mixed coniferous forest naturally regrown from extensive logging during 1900–1910 at US-NR1, conifer forest with scattered herbs and shrubs recovering from logging activity in the early 1900s at US-Me2, very young ponderosa pine stand disturbed by fire and harvest in the 1980s at US-Me3, and a reforested 20-year old ponderosa pine site following fire and salvage cutting at US-Me6. Both upward and downward broadband shortwave solar radiation (0.3–2.8 μm) were measured via Kipp and Zonen (CNR1, CM-3, or CM-6b), or Eppley-PSP tower albedo-meters with 170° effective field of view. Data series collected from the individual sites were processed into the 30-minute standard values, and obtained from the Ameriflux web site: http://ameriflux.ornl.gov. For this study, daily tower albedo values were retrieved corresponding to the Landsat imaging time of 10:30 AM, as well as local solar noon (LSN), the time corresponding to the MODIS MCD43A product suite. In addition, the surface albedo data series (level 2) for site US-NR1 were reviewed for inconsistency during period pre- and post-2005 as a new CNR1 sensor was installed in the fall of 2005. The post-2005 data which were measured with the new well-calibrated sensors were recommended for use by the data provider-(S. Burns, personal communication). An effort to establish sensor-to-sensor cross-calibration is underway, and may provide corrected pre-2005 data soon for further validation activities at US_NR1.

4.1.2. Aggregation from Landsat scale to tower measurement footprint

The disparate spatial scale between satellite and in-situ measurements is one of the barriers to validating satellite-derived products. Several studies have concluded that direct "point-to-pixel" comparison, without considering spatial scales, is not sufficient for albedo product validation, unless the validation focuses on a large and homogenous regions (Liang et al., 2002; Román et al., 2009). The tower based instrument pyranometer is influenced by the "cosine-law" of the response direction and has a 170° effective field of view. An area of $2h \times \tan\left(\frac{85^\circ}{2}\right)$ diameter in the horizontal plane at forest canopy height is then defined by the downward-looking sensor mounted on a tower (h meters above canopy). The calculated diameter of the tower footprint for each site is listed in Table 3. To facilitate the comparison in this study, a cosine-law-based up-scaling method was applied to aggregate the 30-m Landsat albedo to the tower footprint for individual sites (Shuai et al., 2011). The surface albedo corresponding to the tower footprint

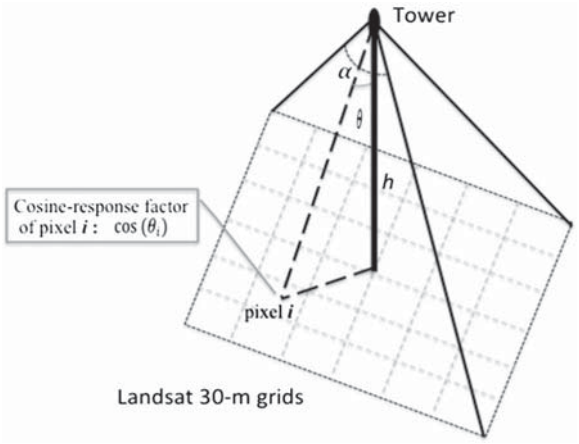

Fig. 6. Illustration of the aggregation from Landsat 30-m pixels (dotted gray grids) into the footprint projected on the ground by albedo meter (FOV = α) mounted on the tower h meters above canopy.

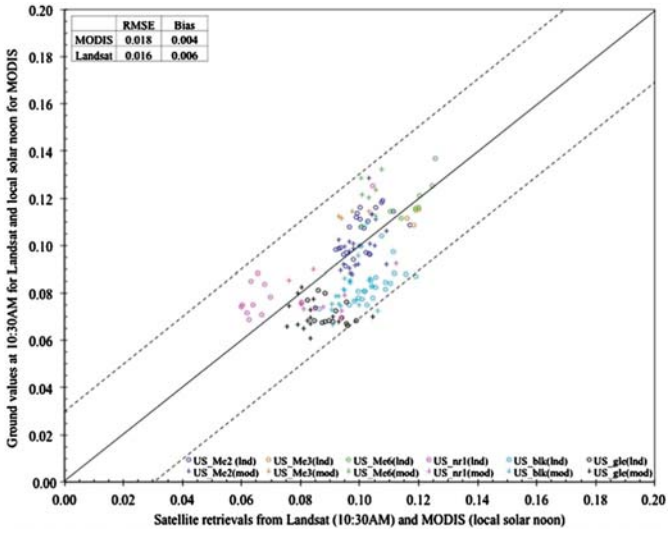

Fig. 7. Comparison of actual (also called blue-sky) shortwave albedo between ground measurements (Y-axis) and satellite retrievals (X-axis) at 10:30 AM from Landsat retrievals and at local solar noon from operational MCD43A3 (V005) products over six AmeriFlux forested sites in Pacific Northwest region of United States, both Landsat and MODIS meet the nominal 0.02 accuracy requirement in root mean square error (Sellers et al., 1995). The dashed lines represent an absolute accuracy of 0.03 compared to the ground data.

$\alpha_{tower\ -\ footprint}$ was obtained as the sum of available 30-m retrievals ($\alpha_{lnd}(i)$) weighted by $\cos(\theta_i)$, where θ_i is the view angle between the tower top and the center of pixel i (Fig. 6) for all the N pixels that fallen in the footprint of ground measurements (Eq. 12).

$$\alpha_{tower-footprint} = \frac{\sum_{i=1}^{N}(\cos(\theta_i) \times \alpha_{lnd}(i))}{\sum_{i=1}^{N}\cos(\theta_i)} \quad (12)$$

4.1.3. Comparison with ground measurement

We derived the surface albedo from the 30-minute tower measured downwelling and upwelling radiation at 10:30 AM for Landsat and at local solar noon for MODIS over each site. Note that retrievals from Landsat as well as MODIS calculate intrinsic surface albedo under two extreme incident radiation situations ("black-sky albedo" corresponding to purely direct solar illumination and "white-sky albedo" corresponding to purely isotropic illumination), while the field measurements record the actual illumination corresponding to a mixture of both direct and diffuse radiation. To obtain comparable metrics with field measurements, we calculate the actual albedo (also called "blue-sky albedo") via the interpolation between black-sky and white-sky albedos weighted by the ratio of direct or diffuse to the total downwelling radiation (Lucht et al., 2000; Román et al., 2011; Schaaf et al., 2002). Since the *in-situ* datasets lack information on direct/diffuse ratios, we simulated the direct/diffuse ratios for required solar zenith angles using 6S based on the simultaneous MODIS Terra atmosphere optical depths at the 550 nm band. Errors induced by the difference of defined wavelength interval for the shortwave band (ground 0.3–3.0 μm, Landsat 0.3–3.0 μm, and 0.3–5.0 μm for MODIS) are negligible because the solar irradiance beyond 2.5 μm accounts for less than 1.8% of the total between 0.3 and 14.3 μm (Hulstrom, Bird, & Riordan, 1985).

The scatter plot (Fig. 7) compares the Landsat blue-sky albedo aggregated to the tower field-of-view with the in-situ measured albedo at 10:30 AM in the shortwave for the six AmeriFlux network sites. Retrievals with snow and cloud contamination were removed from the analysis using the snow and cloud flags in the QA word of the satellite products. The Landsat retrievals are in very good agreement with the tower-based albedo, with a root mean square error (RMSE) less than

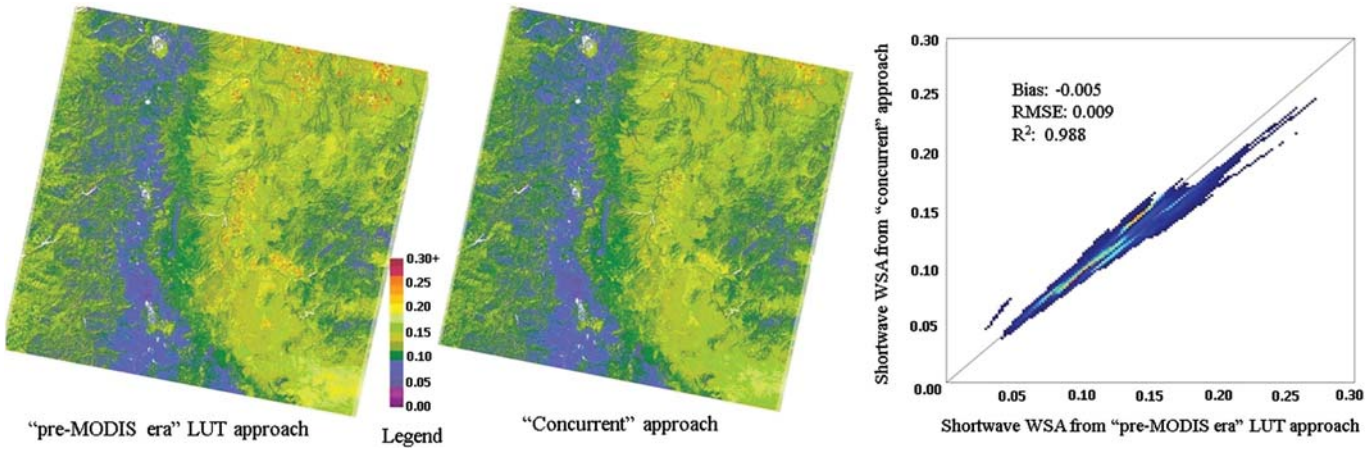

Fig. 8. Cross-comparison of shortwave white-sky albedo map on day 2007-08-29 generated from "pre-MODIS era" LUT approach (left) with "concurrent" approach (middle), and the related scatter plots over all available pixels (right).

0.016 and a bias no more than 0.007. Discrepancy between the Landsat and ground albedos is confined to within ±0.03 albedo (dotted line in Fig. 7), which supports the absolute accuracy requirement (0.02–0.05) established by the climate modeling community (Sellers et al., 1995). Compared with the operational MODIS (V005) shortwave albedo retrievals at local solar noon via the ground measurements as a bridge, the Landsat retrievals are slightly higher, except for the US-NR1 site. This makes sense if we consider the definition of black-sky albedo as described previously. Because values of black-sky albedo depend closely on the direction of solar illumination (i.e. solar zenith angle or timing of observation), and black-sky albedo is commonly observed to decrease from sunrise to noon, then increase from noon to sunset, as validated for MODIS in Liu et al., 2009.

4.2. Cross-comparison with the "concurrent" approach

As an initial validation, we compared albedo maps generated by the "pre-MODIS era" LUT approach to those generated by the previously published "concurrent" approach, which has been validated previously (Román et al., 2013; Shuai et al., 2011). Fig. 8 shows the shortwave broadband white-sky albedo maps derived from both approaches for the identical date 2007-08-29 (fill values excluded in the analysis). The "pre-MODIS era" LUT approach derieved albedo (left) is consistent with that from the "concurrent" approach (right) for the spatial variation of albedo values, from low in the PNW forest region to the high in the eastern barren land. In general, albedo value extracted by the "pre-MODIS era" LUT approach is slightly higher than the "concurrent"

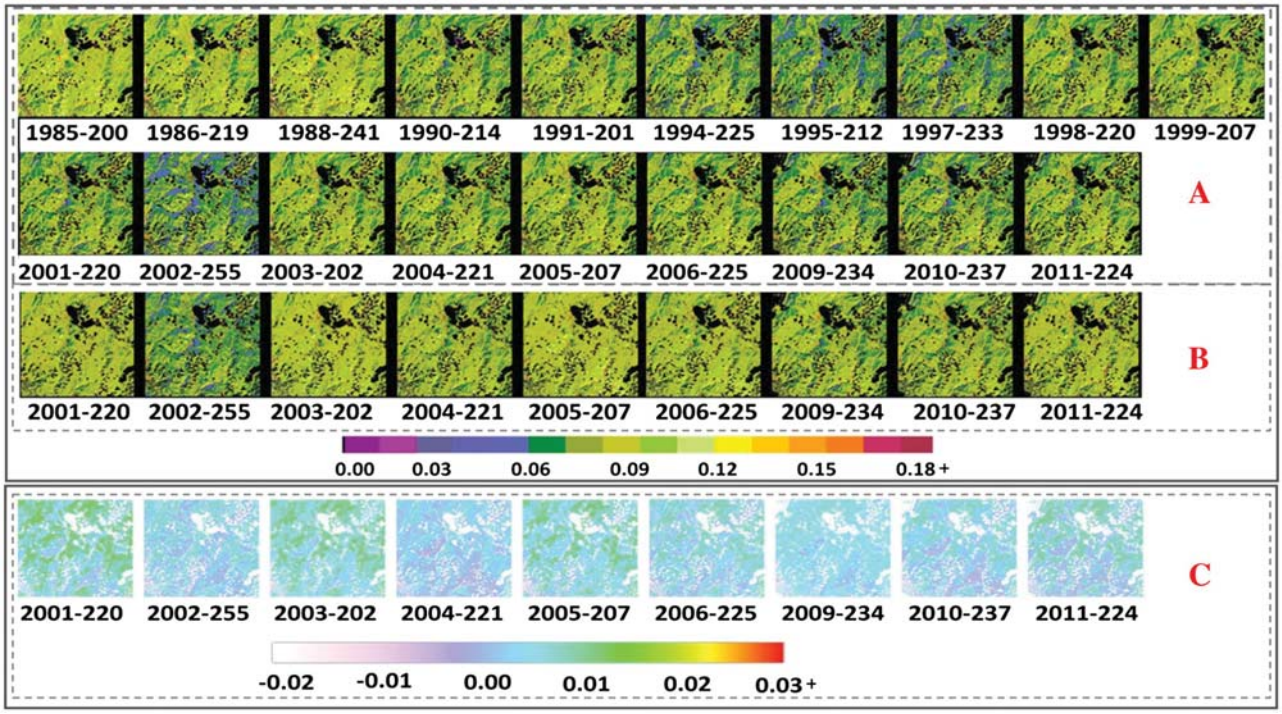

Fig. 9. Illustration of the consistency between the "pre-MODIS era" LUT approach and the "concurrent" approach of Shuai et al. (2011). Shortwave white-sky albedo maps generated respectively from "pre-MODIS era" LUT approach (panel A) and "concurrent" approach (panel B), over an undisturbed forest region in Montana (fill value or disturbed regions in black). The absolute difference maps of white-sky albedo between "concurrent" and "pre-MODIS era" albedo (panel C, fill value or disturbed regions in white) for the overlapping years 2001–2011. Day of year is indicated for each albedo map (YYYY-DOY).

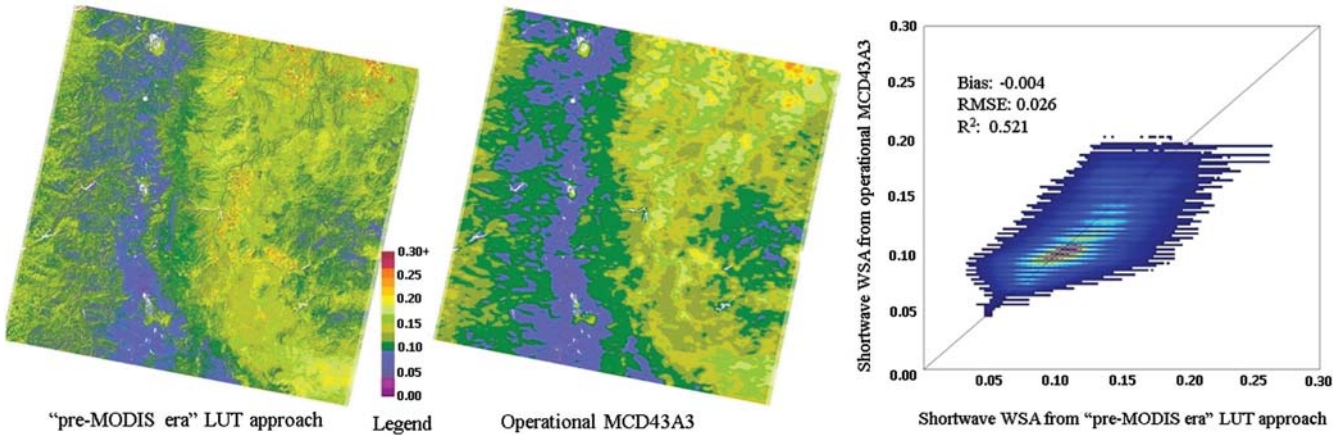

Fig. 10. Cross-comparison of shortwave White-Sky Albedo (WSA) map on day 2007-08-29 generated from "pre-MODIS era" LUT approach (left) with concident MCD43A3 (middle), and the related scatter plot over all available pixels (right).

albedo in some scattered less homogeneous areas in areas of sparse vegetation, which may be due to the difficulty in achieving high quality anisotropy information in fairly heterogeneous localities. However, the pixel-value-based scatter plot (Fig. 8, right) exhibits the good agreement between both approaches with a high R^2 (0.988), a slightly positive bias (0.005) and RMSE (0.009), including a small bias from 1-1 line which is mainly induced by the lack of high quality anisotropy information. The time series of shortwave white-sky albedo retrieved from both approaches at an undisturbed 30 km by 30 km forest region in Montana for the years 1985–2011 and 2001–2011 is displayed in Fig. 9A and B. The consistency over the overlapped summer days of 2001–2011 is displayed in Fig. 9C. The albedo distribution map from both series varies simultaneously with the fluctuation of day-of-year (DOY), exhibiting lower values on day 2002–255 than other earlier DOY. The absolute albedo difference during 2001–2011 for this region is mostly less than 0.01.

4.3. Cross-comparison with MODIS operational product

To further examine the LUT performance, we compared an albedo map generated by the "pre-MODIS" BRDF LUT approach to that produced by the operational MODIS albedo algorithm, which has been extensively validated (Jin et al., 2003; Liu et al., 2009; Román et al., 2009; Wang et al., 2014). To perform the comparison, the MODIS 500-m MCD43A (V005) product was reprojected to the Landsat UTM grid, and resampled to 30-m resolution. Pixels with fill values in either the MODIS or Landsat retrievals were excluded from the analysis. The operational MODIS white-sky albedo for WRS-2 path/row 45/29 was produced for day 2007-08-29 (DOY 241) using the instantaneous BRDF estimate inverted from the 16-day directional observations of days 241–256. The resulting shortwave broadband white-sky albedo (Fig. 10) shows reasonable agreement between the "pre-MODIS era" LUT approach (left) and the MCD43A operational product (middle). The higher spatial resolution of the Landsat retrievals provides greater dynamic range in albedo values. For instance, scattered high values in upper right and central region may be compensated by the surrounding dominant lower values when aggregated to 500 m resolution, resulting in the bright yellowish patch at 500-m resolution. In the scatter plot, the pixel-by-pixel comparison between the "pre-MODIS era" approach and MCD43A reveals the reasonable agreement with dominant points along the one-to-one line, but apparent variation due to the 30-m versus 500-m resolution. In addition, some variance may be introduced by the discrepancy of band passes between Landsat and MODIS.

5. Discussion and conclusions

Our previous study (Shuai et al., 2011) described a "concurrent" approach to retrieving 30-m albedo by combining Landsat directional reflectance with contemporary MODIS BRDF information. Here we have described an approach to extend the generation of albedo products back to the 1980s ("pre-MODIS era") via construction of a priori anisotropy Look-Up Tables (based on modern MODIS data) that may be combined with historical Landsat reflectances. Preliminary LUTs for the Pacific Northwest (PNW) region of the United States were created, with BRDF information stratified by the combination of landscape attributes (land surface, terrain slope, season, and disturbance age and type) for the six non-thermal Landsat-5 and -7. These LUTs provide various BRDF trajectories for undisturbed landscape types and disturbed forest scenarios, including recovery trajectories for fire and non-fire disturbed forest regions. In the future, this approach for the creation of BRDF-LUT could be used to build up LUTs over other regions. With the assumption of generally invariant BRDF shapes for similar land cover conditions, the spectral white-sky and black-sky albedos are derived through albedo-to-nadir reflectance ratios as a bridge between the Landsat and MODIS scales, followed by a narrow-to-broadband conversion to produce the broadband albedos for visible, near infrared, and shortwave spectral regions.

The accuracy of retrieved Landsat albedos were evaluated using available ground measurements at forested AmeriFlux stations in the PNW region and further evaluated through cross-comparison with the surface albedos generated from the "concurrent" approach as well as coincident MODIS operational products. The results show that the retrieved Landsat 30-m shortwave albedo values meet the absolute accuracy of 0.02–0.05 required by climate models at the validation stations (Sellers et al., 1995), and furthermore are consistent with those produced from both "concurrent" approach and MCD43A algorithm. An advantage of the Landsat albedo maps is that the finer resolution results include more detailed representation of the landscape, and a wider dynamic range compared to the 500-m MCD43A product, especially in heterogeneous regions. This is particularly important given the fine-scale landscape patterns that result from both ecosystem disturbance and human modification of land cover.

Future work will expand the validation to structural characteristics across the full range of the North American vegetation regimes by incorporating recent Landsat-based disturbance products (Kennedy et al., 2012; Masek et al., 2013). In addition, with the lengthening MODIS record and the expansion of the detection of disturbance types in the recent disturbance products, we may be able to separate the non-fire disturbance BRDF-LUT into individual disturbance categories, and

reduce the need for BRDF interpolations. Equally important is the incorporation of soil anisotropy once sufficient understanding of natural structured soil anisotropy features are obtained from not only laboratory measurements but also satellite-based estimates. Finally, we intend to develop an approach to retrieve snow-covered albedo at 30-m resolution to further understand the albedo evolution and energy budget over snow covered forest regions.

Acknowledgments

This study was supported by the NASA Terrestrial Ecology Program via a "Science of Terra/Aqua" grant (#NNX11AG53G) and partly by the U.S. Geological Survey (USGS) Landsat science team grant (G12PC00072). The authors would like to thank AmeriFlux network for providing ground data, the extra help on ground details from Drs. Beverly E. Law, Christoph Thomas, William J. Massman, Sean Burns, and Tilden P. Meyers. We thank the LEDAPS project and USGS for providing Landsat surface reflectance, Dr. Zhuosen Wang and the entire MODIS team under NASA grant NNX12AL38G for the generation of operational MCD43A (V005), the Multi-Resolution Land Characteristics (MRLC) consortium to provide NLCD 2006 dataset, the USDA forest service-RSAC and USGS-EROS for the publish of annual MTBS dataset, and Jet Propulsion Laboratory for the open of SRTM data as well University of Maryland for the further process on SRTM and the generation of NAFD data.

References

Bacour, C., & Bréon, F. -M. (2005). Variability of biome reflectance directional signatures as seen by POLDER. *Remote Sensing of Environment*, *98*, 80–95.

Bala, G., Caldeira, K., Wickett, M., Philips, T. J., Lobell, D. B., Delire, C., et al. (2007). Combined climate and carbon-cycle effects of large-scale deforestation. *Proceedings of the National Academy of Sciences*, *104*(16), 6550–6555, http://dx.doi.org/10.1073/pnas.0608998104.

Betts, R. A. (2000). Offset of the potential carbon sink from boreal forestation by decreases in surface albedo. *Nature*, *408*, 187–190.

Bicheron, P., & Leroy, M. (2000). Bidirectional reflectance distribution function signatures of major biomes observed from space. *Journal of Geophysical Research*, *105*, 26669–26681.

Carrer, D., Roujean, J. L., & Meurey, C. (2010). Comparing operational MSG/SEVIRI derived land surface albedo products from Land SAF with ground measurements and MODIS. *IEEE Transactions on Geoscience and Remote Sensing*, *48*(4), 1714–1728.

Cescatti, A., Marcolla, B., Vannan, S. K. S., Pan, J. Y., Román, M. O., Yang, X., et al. (2012). Intercomparison of MODIS albedo retrievals and in situ measurements across the global FLUXNET network. *Remote Sensing of Environment*, *121*, 323–334.

Chen, J. M., & Leblanc, S. G. (1997). A four-scale bidirectional reflectance model based on canopy architecture. *IEEE Transactions on Geoscience and Remote Sensing*, *35*, 1316–1337.

Claussen, M., Brovkin, V., & Ganopolski, A. (2001). Biogeophysical versus biogeochemical feedbacks of large-scale land cover change. *Geophysical Research Letters*, *28*(6), 1011–1014.

Csiszar, I., & Gutman, G. (1999). Mapping global land surface albedo from NOAA/AVHRR. *Journal of Geophysical Research*, *104*(D6), 6215–6228.

Dorman, J. L., & Sellers, P. J. (1989). A global climatology of albedo, roughness length and stomatal resistance for atmospheric general circulation models as represented by the simple biosphere model (SiB). *Journal of Applied Meteorology*, *28*, 833–855.

Eidenshink, J., Schwind, B., Brewer, K., Zhu, Z., Quatle, B., & Howard, S. (2007). A project for monitoring trends in burn severity. *Fire Ecology*, *3*(1), 3–21.

Farr, T. G., et al. (2007). The Shuttle Radar Topography Mission. *Reviews of Geophysics*, *45*, http://dx.doi.org/10.1029/2005RG000183 (RG2004).

Feng, M., Huang, C., Channan, S., Vermote, E. F., Masek, J. G., & Townshend, J. R. (2012). Quality assessment of Landsat surface reflectance products using MODIS data. *Computers & Geosciences*, *38*(1), 9–22, http://dx.doi.org/10.1016/j.cageo.2011.04.0.

Franchistéguy, L., Geiger, B., Roujean, J. -L., & Samain, O. (2005). Retrieval of land surface albedo over France using SPOT4/VEGETATION data. In F. Veroustraete, E. Bartholoé, & W. W. Verstraeten (Eds.), *Proc. 2nd int. VEGETATION user conf.* (pp. 57–62) (Antwerp. Belgium, EUR 21552 EN).

Geiger, B., Carrer, D., Franchisteguy, L., Roujean, J. L., & Meurey, C. (2008). Land surface albedo derived on a daily basis from Meteosat second generation observations. *IEEE Transactions on Geoscience and Remote Sensing*, *46*(2), 3841–3856.

Goward, S. N., Masek, J. G., Cohen, W., Moisen, G., Collatz, G. J., Healey, S., et al. (2008, March 11). Forest disturbance and North American carbon flux. *EOS Transactions*, *89*.

Hall, D. K., Riggs, G. A., & Salomonson, V. V. (1995). Development of methods for mapping global snow cover using Moderate Resolution Imaging Spectroradiometer (MODIS) data. *Remote Sensing of Environment*, *54*, 127–140.

Hall, D. K., Riggs, G. A., Salomonson, V. V., DiGirolamo, N. E., & Bayr, K. J. (2002). MODIS snow-cover products. *Remote Sensing of Environment*, *83*, 181–194.

Hautecoeur, O., & Leroy, M. M. (1998). Surface bidirectional reflectance distribution function observed at global scale by POLDER/ADEOS. *Geophysical Research Letters*, *25*(22), 4197–4200.

He, T., Liang, S., Wang, D., Shuai, Y., & Yu, Y. (2013). Fusion of satellite land surface albedo products across scales using a multiresolution tree method in the north central United States. *IEEE Transactions on Geoscience and Remote Sensing*, http://dx.doi.org/10.1109/TGRS.2013.2272935.

Huang, C., Goward, S. N., Masek, J. G., Thomas, N., Zhu, Z., & Vogelmann, J. E. (2010). An automated approach for reconstructing recent forest disturbance history using dense Landsat time series stacks. *Remote Sensing of Environment*, *114*, 183–198.

Hulstrom, R., Bird, R., & Riordan, C. (1985). *Spectral solar irradiance data sets for selected terrestrial conditions.*

Jin, Y., & Roy, D. P. (2005). Fire-induced albedo change and its radiative forcing at the surface in northern Australia. *Geophysical Research Letters*, *32*, http://dx.doi.org/10.1029/2005GL022822.

Jin, Y., Schaaf, Crystal B., Woodcock, Curtis E., Gao, Feng, Li, Xiaowen, & Strahler, Alan H. (2003). Consistency of MODIS surface bidirectional reflectance distribution function and albedo retrievals: 2. Validation. *Journal of Geophysical Research*, *108*(D5), 4159, http://dx.doi.org/10.1029/2002JD002804.

Ju, J., Roy, D., Shuai, Y., & Schaaf, C. (2010). Development of an approach for generation of temporally complete daily nadir MODIS reflectance time series. *Remote Sensing of Environment*, *114*, 1–20.

Ju, J., Roy, D. P., Vermote, E., Masek, J., & Kovalskyy, V. (2012). Continental-scale validation of MODIS-based and LEDAPS Landsat ETM+ atmospheric correction methods. *Remote Sensing of Environment*, *122*, 175–184.

Justice, C. O., Roman, M. O., Csiszar, I., Vermote, E. F., Wolfe, R. E., Hook, S. J., et al. (2013). Land and cryosphere products from Suomi NPP VIIRS: Overview and status. *Journal of Geophysical Research—Atmospheres*, *118*, 1–13, http://dx.doi.org/10.1002/jgrd.50771.

Kennedy, Rober E., Yang, Zhiqiang, Cohen, Warren B., Pfaff, Eric, Braaten, Justin, & Nelson, Peder (2012). Spatial and temporal patterns of forest disturbance and regrowth within the area of the Northwest Forest Plan. *Remote Sensing of Environment*, *122*, 117–133.

Key, J. R., Wang, J. X., Stroeve, J. C., & Fowler, C. (2001). Estimating the cloudy-sky albedo of sea ice and snow from space. *Journal of Geophysical Research*, *106*(D12), 12489–12497.

Kimes, D. S. (1983). Dynamics of directional reflectance factor distribution for vegetation canopies. *Applied Optics*, *22*(9), 1364–1372.

Kimes, D. S., & Sellers, P. J. (1985). Inferring hemispherical reflectance of the earth's surface for global energy budgets from remotely sensed nadir of directional radiance values. *Remote Sensing of Environment*, *18*, 205–223.

Kimes, D. S., Sellers, P. J., & Newcomb, W. W. (1987). Hemispherical reflectance variations of vegetation canopies and implications for global and regional energy budget studies. *Journal of Climate and Applied Meteorology*, *26*, 959–972.

Leroy, M., Deuze, J. L., Breon, F. M., Hautecoeur, O., Herman, M., Buriez, J. C., et al. (1997). Retrieval of atmospheric properties and surface bidirectional reflectances over land from POLDER/ADEOS. *Journal of Geophysical Research*, *102*, 17 023–17 037.

Lewis, P., & Barnsley, M. J. (1994). Influence of the sky radiance distribution on various formulations of the earth surface albedo. *Proc. Conf. Physics, Measures, and Signals, Val d'Isere, France, 1994* (pp. 707–715).

Li, Z., & Garand, L. (1994). Estimation of surface albedo from space: A parameterization for global application. *Journal of Geophysical Research*, *99*(D4), 8335–8350.

Li, X., & Strahler, A. H. (1992). Geometric-optical bidirectional reflectance modeling of the discrete crown vegetation canopy — Effect of crown shape and mutual shadowing. *IEEE Transactions on Geoscience and Remote Sensing*, *30*, 276–292.

Liang, S. (2000). Narrowband to broadband conversions of land surface albedo: I. *Formulae. Remote Sensing for Environmental Sciences*, *76*, 213–238.

Liang, S. L., Fang, H. L., Chen, M. Z., Shuey, C. J., Walthall, C., Daughtry, C., et al. (2002). Validating MODIS land surface reflectance and albedo products: Methods and preliminary results. *Remote Sensing of Environment*, *83*, 149–162.

Liang, S., Yu, Y., & Defelice, T. P. (2005). VIIRS narrowband to broadband land surface albedo conversion: Formula and validation. *International Journal of Remote Sensing*, *26*(5), 1019–1025.

Liu, J., Schaaf, C., Strahler, A., Jiao, Z., Shuai, Y., Zhang, Q., et al. (2009). Validation of Moderate Resolution Imaging Spectroradiometer (MODIS) albedo retrieval algorithm: Dependence of albedo on solar zenith angle. *Journal of Geophysical Research*, *114*, D01106, http://dx.doi.org/10.1029/2008JD009969.

Loveland, T. R., & Dwyer, J. L. (2012). Landsat: Building a strong future. *Remote Sensing of Environment*, *122*, 22–29.

Lovell, J. L., & Graetz, R. D. (2002). Analysis of POLDER-ADEOS data for the Australian continent: The relationship between BRDF and vegetation structure. *International Journal of Remote Sensing*, *23*(14), 2767–2796.

Lucht, W., Schaaf, C. B., & Strahler, A. H. (March 2000). An algorithm for the retrieval of albedo from space using semiempirical BRDF models. *IEEE Transactions on Geoscience and Remote Sensing*, *38*(2), 977–998.

Lyone, E. A., Jin, Y., & Randerson, J. T. (2008). Changes in surface albedo after fire in boreal forest ecosystems of interior Alaska assessed using MODIS satellite observations. *Journal of Geophysical Research*, *113*, G02012, http://dx.doi.org/10.1029/2007JG000606.

Maignan, F., Breon, F. M., & Lacaze, R. (2004). Bidirectional reflectance of Earth targets: Evaluation of analytical models using a large set of spaceborne measurements with emphasis on the hot spot. *Remote Sensing of Environment*, *90*(2), 210–220.

Martonchik, J. V., Diner, J. V., Pinty, D. J., Verstraete, M. M., Myneni, R. B., Knyazikhim, Y., et al. (1998). Determination of land and ocean reflective, radiative, and biophysical properties using multiangle imaging. *IEEE Transactions on Geoscience and Remote Sensing*, *36*(4), 1266–1281.

Martonchik, J. V., Pinty, B., & Verstraete, M. M. (2002). Note on an improved model of surface BRDF-atmospheric coupled radiation. *IEEE Transactions on Geoscience and Remote Sensing*, *40*(7), 1637–1639.

Masek, J. G., & Collatz, G. J. (2006). Estimating forest carbon fluxes in a disturbed southeastern landscape: Integration of remote sensing, forest inventory, and biogeochemical modeling. *Journal of Geophysical Research*, *111*, G01006, http://dx.doi.org/10.1029/2005JG000062.

Masek, J. G., Goward, S. N., Kennedy, R. E., Cohen, W. B., Moisen, G. G., Schleeweis, K., et al. (2013). United States forest disturbance trends observed using Landsat time series. *Ecosystems*, http://dx.doi.org/10.1007/s10021-013-9669-9.

Masek, J. G., Huang, C. Q., Wolfe, R., Cohen, W., Hall, F., Kutler, J., et al. (2008). North American forest disturbance mapped from a decadal Landsat record. *Remote Sensing of Environment*, *112*(6), 2914–2926.

Masek, J. G., Vermote, E. F., Saleous, N. E., Wolfe, R., Hall, F. G., Huemmrich, K. F., et al. (2006). A Landsat surface reflectance dataset for North America, 1990–2000. *Geoscience and Remote Sensing Letters*, *3*, 68–72.

Nicodemus, F. E., Richmond, J. C., Ginsberg, I. W., & Limperis, T. (1977). *Geometrical considerations and nomenclature for reflectance. NBS Monograph*, *160*, Washington, DC: National Bureau of Standards, U. S. Department of Commerce.

O¡¯Halloran, T., Law, B., Goulden, M. L., Wang, Z., Barr, J., & Schaaf, C. (2011). Radiative forcing of natural forest disturbances. *Global Change Biology*, http://dx.doi.org/10.1111/j.1365-2486.2011.02577.x.

Ollinger, S. V., Richardon, A. D., Martin, M. E., Hollinger, D. Y., Frolking, S. E., Reich, P. B., et al. (2008). Canopy nitrogen, carbon assimilation, and albedo in temperate and boreal forests: Functional relations and potential climate feedbacks. *Proceedings Natonal Academy of Sciences*, *105*, 19336–19341.

Pan, Y., Birdsey, R. A., Fang, J., Houghton, R., Kauppi, P. E., Kurz, W. A., et al. (2011). A large and persistent carbon sink in the world's forests. *Science*, *333*, 988–993.

Peckham, S. D., Ahl, D. E., Serbin, S. P., & Gower, S. T. (2008). Fire-induced changes in green-up and leaf maturity of the Canadian boreal forest. *Remote Sensing of Environment*, *112*, 3594–3603.

Pinty, B., Lavergne, T., Kaminski, T., Aussedat, O., Giering, R., Gobron, N., et al. (2008). Partitioning the solar radiant fluxes in forest canopies in the presence of snow. *Journal of Geophysical Research*, *113*, D04104, http://dx.doi.org/10.1029/2007JD009096.

Pinty, B., Roveda, F., Verstraete, M. M., Gobron, N., Govaerts, Y., Martonchik, J. V., et al. (2000). Surface albedo retrieval from METEOSAT part 1: Theory. *Journal of Geophysical Research*, *105*(D14), 18099–18112.

Privette, J. L., Eck, T. F., & Deering, D. W. (1997). Estimating spectral albedo and nadir reflectance through inversion of simple BRDF models with AVHRR/MODIS-like data. *Journal of Geophysical Research*, *102*, 29529–29542.

Randerson, J. T., Liu, H., Flanner, M. G., Chambers, S. D., Jin, Y., & Hess, P. G. (2006). The impact of boreal forest fire on climate warming. *Science*, *314*, 1130–1132.

Román, M. O., Gatebe, C. K., Schaaf, C. B., Poudyal, R., Wang, Z., & King, M. D. (2011). Variability in surface BRDF at different spatial scales (30 m - 500 m) over a mixed agricultural landscape as retrieved from airborne and satellite spectral measurements. *Remote Sensing of Environment*, *115*, 2184–2203.

Román, M. O., Gatebe, C. K., Shuai, Y., Wang, Z., Gao, F., Masek, J., et al. (2013). Use of in situ and airborne multiangle data to assess MODIS- and Landsat-based estimates of directional reflectance and surface albedo. *IEEE Transactions on Geoscience and Remote Sensing*, *51*(3), 1393–1404.

Román, M. O., Schaaf, C. B., Lewis, P., Gao, F., Anderson, G. P., Privette, J. L., et al. (2010). Assessing the coupling between surface albedo derived from MODIS and the fraction of diffuse skylight over spatially-characterized landscapes. *Remote Sensing of Environment*, *114*, 738–760.

Román, M. O., Schaaf, C. B., Woodcock, C. E., Strahler, A. H., Yang, X., Braswell, R. H., et al. (2009). The MODIS (Collection V005) BRDF/albedo product: Assessment of spatial representativeness over forested landscapes. *Remote Sensing of Environment*, *113*(11), 2476–2498.

Ross, J. (1981). The radiation regime and architecture of plant stands. Norwell, Mass: The Hague: Dr. W. Junk Publishers.

Roujean, J. -L., Leroy, M., Podaire, A., & Deschamps, P. Y. (1992). Evidence of surface reflectance bidirectional effects from a NOAA/AVHRR multitemporal dataset. *International Journal of Remote Sensing*, *13*, 685–698.

Ruehr, N. K., Martin, J. G., & Law, B. E. (2012). Effects of water availability on carbon and water exchange in a young ponderosa pine forest: Above- and belowground responses. *Agricultural and Forest Meteorology*, *164*, 136–148.

Rutan, D., Rose, F., Román, M., Manalo-Smith, N., Schaaf, C., & Charlock, T. (2009). Development and assessment of broadband surface albedo from clouds and the Earth's radiant energy system clouds and radiation swath data product. *Journal of Geophysical Research*, *114*, D08125, http://dx.doi.org/10.1029/2008JD010669.

Schaaf, C. B., Cihlar, J., Belward, A., Dutton, E., & Verstraete, M. (2009 Mayy). In R. Sessa (Ed.), *Albedo and reflectance anisotropy, ECV-T8: Assessment of the status of the development of standards for the terrestrial essential climate variables*. Rome: FAO.

Schaaf, C. B., Gao, F., Strahler, A. H., Lucht, W., Li, X., Tsang, T., et al. (2002). First operational BRDF, albedo and nadir reflectance products from MODIS. *Remote Sensing of Environment*, *83*, 135–148.

Schaaf, C. Barker, Li, X., & Strahler, A. H. (1994). Topographic effects on bidirectional and hemispherical reflectances calculated with a geometric-optical model. *IEEE Transactions on Geoscience and Remote Sensing*, *32*, 1186–1193.

Schaaf, C. L. B., Liu, J., Gao, F., & Strahler, A. H. (2011). MODIS albedo and reflectance anisotropy products from Aqua and Terra. In B. Ramachandran, C. Justice, & M. Abrams (Eds.), *Land remote sensing and global environmental change: NASA's earth observing system and the science of ASTER and MODIS. Remote Sensing and Digital Image Processing Series*, *Vol.11*. (pp. 873). Springer-Cerlag.

Schaaf, C. L., Martonchik, J., Pinty, B., Govaerts, Y., Gao, F., Lattanzio, A., et al. (2008). Retrieval of surface albedo from satellite sensors. In S. Liang (Ed.), *Advances in land remote sensing: System, modeling, inversion and application* (pp. 219–243). Springer978-1-4020-6449-4.

Schaepman-Strub, G., Schaepman, M. E., Painter, T. H., Dangel, S., & Martonchik, J. V. (2006). Reflectance quantities in optical remote sensing — Definitions and case studies. *Remote Sensing of Environment*, *103*, 27–42.

Sellers, P. J., Los, S. O., Tucker, C. J., Justice, C. O., Dazlich, D. A., Collatz, G. J., et al. (1996a). A revised land surface parameterization (SiB2) for atmospheric GCMs. 2. The generation of global fields of terrestrial biophysical parameters from satellite data. *Journal of Climate*, *9*, 706–737.

Sellers, P. J., Meeson, B. W., Hall, F. G., Asrar, G., Murphy, R. E., Schiffer, R. A., et al. (1995). Remote sensing of the land surface for studies of global change: Models &algorithms experiments. *Remote Sensing of Environment*, *15*(1), 3–26.

Sellers, P. J., Randall, D. A., Collatz, G. J., Berry, J. A., Field, C. B., Dazlich, D. A., et al. (1996b). A revised land surface parameterization (SiB2) for atmospheric GCMs. 1. Model formulation. *Journal of Climate*, *9*, 676–705.

Shuai, Y., Masek, J. G., Gao, F., & Schaaf, C. B. (2011). An algorithm for the retrieval of 30-m snow free albedo from Landsat surface reflectance and MODIS BRDF. *Remote Sensing of Environment*, *115*, 2204–2216.

Shuai, Y., & Schaaf, C. B. (2010). *Tracking daily land surface albedo and reflectance anisotropy with moderate-resolution imaging spectroradiometer (MODIS)*. Dissertation. Boston University (2010.2010.3382585).

Shuai, Y., Schaaf, C. B., Strahler, A. H., Liu, J., & Jiao, Z. (2008). Quality assessment of BRDF/albedo retrievals in MODIS operational system. *Geophysical Research Letters*, *35*, L05407, http://dx.doi.org/10.1029/2007GL032568.

Shuai, Y., Schaaf, C., Zhang, X., Strahler, A., Roy, D., Morisette, J., et al. (2013a). Daily MODIS 500 m reflectance anisotropy direct broadcast (DB) products for monitoring vegetation phenology dynamics. *International Journal of Remote Sensing*, *34*, 5997–6016.

Shuai, Y., Xie, D., Wang, P., & Wu, M. (2013b). Understanding of crop phenology using satellite-based retrievals and climate factors—Case study on spring maize in Northeast China plain. *35th International Symposium on Remote Sensing of Environment (ISRSE), Beijing, China, April, 2013*.

Strahler, A. H., Wanner, W., Schaaf, C. B., Li, X., Hu, B., Muller, J. -P., et al. (1999, April). *MODIS BRDF/albedo product: Algorithm theoretical basis document.* (Version 5.0.).

Strugnell, N. C., & Lucht, W. (2001). An algorithm to infer continental-scale albedo from AVHRR data, land cover class, and field observations of typical BRDFs. *Journal of Climate*, *14*, 1360–1376.

Thomas, C. K., Law, B. E., Irvine, J., Martin, J. G., Pettijohn, J. C., & Davis, K. J. (2009). Seasonal hydrology explains inter-annual and seasonal variation in carbon and water exchange in a semi-arid mature ponderosa pine forest in central Oregon. *Journal of Geophysical Research — Biogeosciences*, *114*, G04006.

Townshend, J. R. G., & Justice, C. O. (1988). Selecting the spatial resolution of satellite sensors required for global monitoring of land transformations. *International Journal of Remote Sensing*, *9*, 187–236.

Vermote, E. F., ElSaleous, N., Justice, C. O., Kaufman, Y. J., Privette, J. L., Remer, L., et al. (1997). Atmospheric correction of visible to middle-infrared EOS-MODIS data over land surfaces: Background, operational algorithm and validation. *Journal of Geophysical Research — Atmospheres*, *102*(D14), 17131–17141.

Vermote, E. F., Saleous, N., & Justice, C. O. (2002). Atmospheric correction of MODIS data in the visible to middle infrared: First results. *Remote Sensing of Environment*, *83*(1–2), 3–15.

Vickers, D., Thomas, C. K., Pettijohn, C., Martin, J. G., & Law, B. E. (2012). Five years of carbon fluxes and inherent water-use efficiency at two semi-arid pine forests with different disturbance histories. *Tellus B*, *64*, 17159.

Vogelmann, J. E., Sohl, T., & Howard, S. M. (1998). Regional characterization of land cover using multiple sources of data. *Photogrammetric Engineering & Remote Sensing*, *64*(1), 45–47.

Wang, Z., Schaaf, C. B., Strahler, A. H., Chopping, M. J., Román, M. O., Shuai, Y., et al. (2014). Evaluation of MODIS albedo product (MCD43A) over grassland, agriculture and forest surface types during dormant and snow-covered periods. *Remote Sensing of Environment*, *140*, 60–77.

Wickham, J. D., Stehman, S. V., Gass, L., Dewitz, J., Fry, J. A., & Wade, T. G. (2013). Accuracy assessment of NLCD 2006 land cover and impervious surface. *Remote Sensing of Environment*, *130*, 294–304.

Wilson, T. B., & Meyers, T. P. (2007). Determining vegetation indices from solar and photosynthetically active radiation fluxes. *Agricultural and Forest Meteorology*, *144*, 160–179.

Woodcock, C. E., Allen, R., Anderson, M., Belward, A., Bindschadler, R., Cohen, W. B., et al. (2008). Free access to Landsat imagery. *Science*, *320*, 1011, http://dx.doi.org/10.1126/science.320.5879. 1011a.

Wulder, M. A., Masek, J. G., Cohen, W. B., Loveland, T. R., & Woodcock, C. E. (2012). Opening the archive: How free data has enabled the science and monitoring promise of Landsat. *Remote Sensing of Environment*, *122*, 2–10.

Xu, L., Myneni, R. B., Chapin, F. S., III, Callaghan, T. V., Pinzon, J. E., Tucker, C. J., et al. (2013). Temperature and vegetation seasonality diminishment over northern lands. *Nature Climate Change*, http://dx.doi.org/10.1038/NCLIMATE1836.

Zhang, Q., Middleton, E. M., Margolis, H. A., Drolet, G. G., Barr, A. A., & Andrew, Black T. (2009). Can a satellite-derived estimate of the fraction of PAR absorbed by chlorophyll (FAPARchl) improve predictions of light-use efficiency and ecosystem photosynthesis for a boreal aspen forest? *Remote Sensing of Environment*, *113*, 880–888.